The Astrophysical Journal, 930:172 (9pp), 2022 May 10 https://doi.org/10.3847/1538-4357/ac63a8

Simultaneous View of FRB 180301 with FAST and NICER during a Bursting Phase

Sibasish Laha[1,2,3], George Younes[2], Zorawar Wadiasingh[2,3,4], Bo-Jun Wang[5,6,7], Ke-Jia Lee[5,7], Noel Klingler[1,2,3], Bing Zhang[8,9], Heng Xu[5,6,7], Chun-Feng Zhang[5,6,7], Wei-Wei Zhu[7], Ritesh Ghosh[10], Amy Lien[11], Eleonora Troja[2,12], S. Bradley Cenko[2,13], Samantha Oates[14,15], Matt Nicholl[14,15], Josefa Becerra González[16,17], Eileen Meyer[18], and Tyler Parsotan[1,2,3]

[1] Center for Space Science and Technology, University of Maryland Baltimore County, 1000 Hilltop Circle, Baltimore, MD 21250, USA; sibasish.laha@nasa.gov, sib.laha@gmail.com
[2] Astrophysics Science Division, NASA Goddard Space Flight Center, Greenbelt, MD 20771, USA
[3] Center for Research and Exploration in Space Science and Technology, NASA/GSFC, Greenbelt, Maryland 20771, USA
[4] Department of Astronomy, University of Maryland, College Park, Maryland 20742, USA
[5] Kavli Institute for Astronomy and Astrophysics, Peking University, Beijing 100871, People's Republic of China
[6] Department of Astronomy, School of Physics, Peking University, Beijing 100871, People's Republic of China
[7] National Astronomical Observatories, Chinese Academy of Sciences, Beijing 100101, People's Republic of China
[8] Department of Physics and Astronomy, University of Nevada Las Vegas, Las Vegas, NV 89154 USA
[9] Nevada Center for Astrophysics, University of Nevada, Las Vegas, NV 89154, USA
[10] Inter-University Centre for Astronomy and Astrophysics (IUCAA), Pune, 411007, India
[11] University of Tampa, Department of Chemistry, Biochemistry, and Physics, 401 West Kennedy Boulevard, Tampa, FL 33606, USA
[12] University of Rome–Tor Vergata, Department of Physics, via della Ricerca Scientifica 1, 00100, Rome, Italy
[13] Joint Space-Science Institute, University of Maryland, College Park, MD 20742, USA
[14] School of Physics and Astronomy, University of Birmingham, Birmingham B15 2TT, UK
[15] Institute for Gravitational Wave Astronomy, University of Birmingham, Birmingham B15 2TT, UK
[16] Instituto de Astrofísica de Canarias (IAC), E-38200 La Laguna, Tenerife, Spain
[17] Universidad de La Laguna (ULL), Departamento de Astrofísica, E-38206 La Laguna, Tenerife, Spain
[18] Department of Physics, University of Maryland, Baltimore County, 1000 Hilltop Circle, Baltimore, MD 21250, USA
Received 2021 December 17; revised 2022 March 29; accepted 2022 March 30; published 2022 May 17

Abstract

FRB 180301 is one of the most actively repeating fast radio bursts (FRBs) that has shown polarization angle changes in its radio burst emission, an indication for their likely origin in the magnetosphere of a highly magnetized neutron star. We carried out a multiwavelength campaign with the FAST radio telescope and NICER X-ray observatory to investigate any possible X-ray emission temporally coincident with the bright radio bursts. The observations took place on 2021 March 4, 9 and 19. We detected five bright radio bursts with FAST, four of which were strictly simultaneous with the NICER observations. The peak flux density of the radio bursts ranged between 28 and 105 mJy, the burst fluence between 27 and 170 mJy ms, and the burst durations between 1.7 and 12.3 ms. The radio bursts from FRB 180301 exhibited a complex time domain structure, and subpulses were detected in individual bursts, with no significant circular polarization. The linear degree of polarization in the L band reduced significantly compared to the 2019 observations. We do not detect any X-ray emission in excess of the background during the 5, 10, 100 ms, 1 and 100 s time intervals at/around the radio-burst barycenter-corrected arrival times, at a $> 5\sigma$ confidence level. The 5σ upper limits on the X-ray (a) persistent flux is $<7.64 \times 10^{-12}$ erg cm^{-2} s^{-1}, equivalent to $L_X < 2.50 \times 10^{45}$ erg s^{-1} and (b) 5 ms fluence is $<2 \times 10^{-11}$ erg cm^{-2}, at the radio burst regions. Using the 5 ms X-ray fluence upper limit, we can estimate the radio efficiency $\eta_{R/X} \equiv L_{\rm radio}/L_{\rm X-ray} \gtrsim 10^{-8}$. The derived lower limit on $\eta_{R/X}$ is consistent with both magnetospheric models and synchrotron maser models involving relativistic shocks.

Unified Astronomy Thesaurus concepts: Radio transient sources (2008)

1. Introduction

Fast radio bursts (FRBs) are millisecond-duration radio pulses whose origin is still highly debated (Lorimer et al. 2007; Tendulkar et al. 2017; CHIME/FRB Collaboration et al. 2019a; Petroff et al. 2019; Zhang 2020; Caleb & Keane 2021; Sridhar et al. 2021). Recently, large radio surveys have detected several new FRBs, some of which have shown repeating emission, implying an origin that does not involve one-time cataclysmic events, such as neutron star mergers (CHIME/FRB Collaboration et al. 2019a). These repeating FRBs are interesting because they may be scrutinized in different parts of the electromagnetic spectrum over long periods of time, to attempt to reveal the physical nature of the FRB engine. One such repeating FRB (but apparently not periodic in activity) in the CHIME/FRB catalog is FRB 20180301A (hereafter FRB 180301), which was first detected by the Parkes 64 m radio telescope, and has a dispersion measure (DM) of 522 cm^{-3} pc. Bhandari et al. (2022) identified PSO J093.2268+04.6703 as the putative host galaxy of FRB 180301. The host of FRB 180301 is located at a redshift of $z = 0.334$, implying a luminosity distance of ~1.7 Gpc. The Five-hundred-meter Aperture Spherical radio Telescope (FAST), which is the largest single dish radio telescope with high sensitivity, observed this source in 2019 July, September, and October for a total of 12 hr (Luo et al. 2020). The bursts detected from FRB 180301 had peak flux densities ranging from 5.3–94.1 mJy. All the bursts exhibit a high degree of linear polarization, and no circular polarization was detected even for the highest signal-to-noise bursts. This

property is similar to the other actively repeating FRB 121102, which exhibits ∼100% linear polarization (Michilli et al. 2018).

Most interestingly, a considerable amount of diversity in the polarization angle (PA) swings across the pulse profile were detected by FAST for FRB 180301, which implies that the bursts are consistent with an origin from a neutron star magnetosphere and disfavors far-flung relativistic shocks (Luo et al. 2020). The change in the PA from one burst to another in the same source indicates that the radiation is produced within the light cylinder of a strongly magnetized neutron star. As the emitted radiation travels through the magnetosphere, the electric vector of the X-mode wave adiabatically rotates and stays perpendicular to the local magnetic field direction (the O mode is approximately a normal mode of the plasma). The PA freezes at a radius where the plasma density becomes too small to be able to turn the electric vector. At the *freeze-out radius*, the electric field is perpendicular to the magnetic dipole moment of the neutron star projected in the plane of the sky, independent of the radiation mechanism or the orientation of the magnetic field in the emission region. The changes in the PAs from FRB 180301 should therefore, trace the rotational period of the underlying neutron star.

Magnetars have been historically strongly suspected as progenitors of FRBs (Popov & Postnov 2010, 2013; Kulkarni et al. 2014; Lyubarsky 2014; Katz 2016; Beloborodov 2017; Kumar et al. 2017; Yang & Zhang 2018; Metzger et al. 2019; Wadiasingh & Timokhin 2019). The recent detection of FRB 200428 (Bochenek et al. 2020; CHIME/FRB Collaboration et al. 2020) temporally coincident with a hard X-ray (20−200 keV) burst (Mereghetti et al. 2020; Li et al. 2021) from magnetar SGR 1935+2154 (SGR 1935 hereafter) in April 2020 confirmed that at least some of the FRBs are produced by magnetar bursts. The radio to X-ray data have been interpreted within the magnetar framework in several competing models (e.g., Lu et al. 2020; Margalit et al. 2020; Wadiasingh & Chirenti 2020; Yang & Zhang 2021; Zhang 2022). On the other hand, the FRB luminosity detected from SGR 1935 is very low in comparison to its extragalactic counterparts, prompting yet another question of whether Galactic and extragalactic FRBs indeed have the same origin. Nevertheless, the association of the FRBs with magnetars has prompted several dedicated searches of X-ray counterparts with current X-ray observatories. One of the important steps to test magnetar or shocked-outflow models is to estimate the ratio of energy emitted in the FRBs over that in other bands (such as in X-rays), measured by the efficiency factor $\eta_{R/X} \equiv E_{\rm radio}/E_{\rm X\text{-}ray}$. In some magnetar models, this ratio is much less than unity, typically $\sim 10^{-3}$–10^{-7} (e.g., Lu et al. 2020; Margalit et al. 2020; Yang & Zhang 2021). Therefore, strong limits on η can challenge or confirm several models.

Following the discovery of the changes in the PA in the source FRB 180301 (Luo et al. 2020), we carried out a simultaneous radio-X-ray campaign in 2021 March, with FAST and The Neutron Star Interior Composition Explorer Mission (NICER) telescopes to capture any X-ray emission temporally coincident with the radio bursts during the bursting phases of the FRB. There were five radio bursts from FRB 180301 during the multiwavelength observational campaign and in this work we report a detailed analysis of the radio and X-ray observations. This paper is arranged as follows: Section 2 discusses the radio and X-ray observations and data analysis. Section 3 lists the main results followed by discussion and summary in Section 4, respectively.

Table 1
Simultaneous NICER Observations of FRB 180301 in 2021 March

NICER-obsid	Obs Number	Date	Total Exposure (s)	FRB Detected?
4533020101	obs1	2021 Mar 4	1998	No
4533020102	obs2	2021 Mar 9	4347	Yes
4533020103	obs3	2021 Mar 19	7151	Yes

2. Observations and Data Reduction

FAST (Nan et al. 2011) and NICER (Gendreau et al. 2016) observed FRB 180301 on 2021 March 4, 9, and 19. See Tables 2 and 1 for the FAST and NICER observation details, respectively. During these observations, four radio bursts were strictly contemporaneous. Since this work is focused on NICER+FAST simultaneous monitoring of FRB 180301, we did not study other wavelength bands (or observations from other telescopes) for this FRB in this work. Below we describe the methods involved in data reprocessing and analysis of the radio and X-ray observations of FRB 180301.

2.1. FAST Observations

The radio observations were carried out using FAST, of which the effective collecting area is 196,000 m^2 (Nan et al. 2011). We used the central beam of the 19-beam receiver to observe. In the frequency coverage of 1000–1500 MHz, the system temperature is 20–25 K (Jiang et al. 2020). Observed data were recorded using the digital backend based on the Re-configurable Open Architecture Computing Hardware-2 (ROACH2) board (Hickish et al. 2016), where the search data (i.e., the intensity or audio data) is formed via polyphase filter banks and time integration on a XILINX Virtex-6 family field-programmable gate array chip. The final temporal and frequency resolutions are 49.152 μs and 122.07 kHz, respectively.

We searched for the FRB candidates offline with the recorded filter bank data. The two 20 MHz band edges, i.e., 1000–1020 MHz and 1480–1500 MHz were removed due to the loss of sensitivity and rapid change of signal phase. Frequency channels, which were affected by satellite RFIs in the ranges of 1200–1210 MHz and 1265–1280 MHz, were also removed. The software package BEAR (Burst Emission Automatic Roger; Men et al. 2019) is used to search for FRB candidates. Since FRB 180301 is a known repeater, we searched with a narrow DM range of 508–528 pc cm^{-3}. We searched for pulses with a pulse width range of 0.2–30 ms. Candidates with a signal-to-noise ratio (S/N) larger than 6 were recorded to evaluate the red noise effects as explained in Zhang et al. (2021). Bursts with a S/N larger than 7 will be visually inspected and reported in this paper. In this way, the chance of a burst being artifact is less than 3×10^{-6}, assuming 10% red noise power. Five bursts were detected in our observation with detailed information listed in Table 2.

After detection, the DM is further refined using the phase coherence spectral techniques (CHIME/FRB Collaboration et al. 2019b), which optimize the burst sharpness instead of maximizing the pulse S/N.

We estimate the pulse flux assuming a 22 K system temperature, the major error of flux comes from the noise temperature variation, which is 20% as measured in the FAST engineering phase. We calculate the mean flux using

Table 2
Radio Bursts from FRB 180301 Detected by FAST during the Joint FAST-NICER Campaign in 2021 March

Idx N	Barycentric TOA(MJD)	Date	Peak Flux Density mJy	Mean Flux Density mJy	Width . ms	S/N
1	59282.462719811028261	2021 Mar 9	79	18	12.3 ± 0.4	44
2	59282.519910811797640	2021 Mar 9	44	16	4.1 ± 0.2	21
3	59282.526543512274323	2021 Mar 9	28	16	1.7 ± 0.2	11
4	59292.407031067837291	2021 Mar 19	105	47	4.10 ± 0.06	69
5	59292.411839390156917	2021 Mar 19	60	18	7.9 ± 0.2	36

Note: (a) The major error of flux measurement comes from system temperature drift, which is approximately 20%. (b) The pulse width is defined as $(8 \ln 2)^{1/2}$ of the *intensity weighted width*, which agrees with the definition of the FWHM for Gaussian profiles.

radiometer equation

$$S_{\min} = \beta \frac{(\mathrm{S/N}) \cdot T_{\mathrm{sys}}}{G\sqrt{N_p W_{\mathrm{eq}} \Delta\nu}}, \quad (1)$$

where W is the pulse width, correction factor $\beta \approx 1$, and $N_p = 2$ is the number of polarization channels. System temperature $T_{\mathrm{sys}} \approx 22$ K and gain $G = 16$ K Jy^{-1} for FAST. Neglecting the intrinsic bandwidth of FRB, we calculate, hereafter, the band-averaged flux and the bandwidth $\Delta\nu$ is fixed to be 400 MHz.

We perform polarization calibration using software PSRCHIVE with the single-axial model (Hotan et al. 2004), i.e., we neglected the leakage terms, which are measured as low as -46 dB. As will be discussed shortly, the linear polarization is very weak compared to previous observations. We only plot the total intensity pulse profiles and de-dispersed dynamic spectra as shown in Figure 1.

The barycentric *infinite-frequency equivalent* time of arrivals are computed using TEMPO2 (Hobbs et al. 2006), where Römer delay, relativity delay in the solar system, and dispersive time delay were corrected. In the process, we have adopted the position of R.A.$06^{\mathrm{h}}12^{\mathrm{m}}54.51^{\mathrm{s}}$, and decl. $+04°40'15.''4$ as measured with Karl G. Jansky Very Large Array (VLA; Bhandari et al. 2022). We understand that there may be an offset of approximately 2 mas between the The International Celestial Reference Frame used by VLA and solar system dynamic coordinate used by Tempo2 (Wang et al. 2017), the corresponding error in timing is 4.8 μs, which is negligibly small compared to the error of the measured pulse width.

As in Figure 1, the radio pulse profiles of FRB 180301 can be hardly described by Gaussian-like curves. We thus measure the pulse profile using the intensity weighted width, i.e., we treat the pulse profile as the temporal intensity distribution function, and calculate the standard deviation of time. A correction factor of $(8 \ln 2)^{1/2}$ is multiplied to the standard derivation when we report the pulse width. The factor is introduced such that the intensity weighted width will be the FWHM for Gaussian profiles.

2.2. NICER Observations

NICER was launched in 2017 and is currently working as one of the payloads on the International Space Station (ISS). NICER consists of one instrument, the X-ray Timing Instrument, which operate in the soft X-ray band (0.2–12 keV). The data files for the three NICER observations (PI: S. Laha, see Table 1) were downloaded from HEASARC, and were reduced using the standard NICER procedure. The raw data were processed using the NICERDAS software package (version 2021-08-31_V008c) in HEASOFT (v6.29c), using the latest caldb version.

We created cleaned event files by applying the standard calibration and filtering tool, `nicerl2` to the unfiltered data using the default values, and then performed barycenter corrections using `barycorr`. We restricted events to the 0.3–12 keV range. To remove excess background noise from the time periods surrounding NICER's passages through the South Atlantic Anomaly (SAA), we binned the data into 16 s bins and filtered out intervals where the count rate exceeded 1.4 counts s^{-1} in `XSELECT`. This was done to obtain NICER steady background rate. Although we note that two of the bursts (bursts 1 and 3) happened in the wings when the spacecraft was coming out of the SAA. We then used `XSELECT` to extract light curves and spectra from the filtered data. We have used the latest response file, nixtiref20170601v002.rmf, for the spectral analysis. Note that we do not use the NICER observation 1 for further analysis in this paper because it was not simultaneous with any radio burst from FRB 180301, and also the net exposure (after filtering) was only 700 s, and hence the signal to noise was insufficient to carry out a detailed timing and spectral analysis.

We used Xselect to obtain the time averaged spectra for the two NICER observations. After plotting the source+background spectra, along with the modeled background spectra estimated using the `nicerbackgen` software, we did not find any excess emission above the background.

3. Results

3.1. Radio Burst Properties

In the radio band, FRB 180301 exhibited complex time domain structure. Subpulses where detected in single bursts. As also detected in other repeating FRBs, subpulse frequency drifting is visible in the dynamic spectra of burst 4 and probably in bursts 1 and 2.

There is no significant circular polarization in the pulse we detected as in the previous observation (Luo et al. 2020). Furthermore, we note that the linear degree of polarization in L band reduced significantly in the 2021 March observations. The degree of linear polarization dropped to less than 10%, while it was as high as 80% in 2019. The change in the observed polarization properties may be related to the propagation effects of the FRBs, and may probe the immediate environment around the FRB source (Xu et al. 2021; Feng et al. 2022). However, no significant change in the high energy emission properties, which depend on the intrinsic radiation mechanism, is expected. A detailed analysis of polarization properties is

Table 3
X-Ray Flux and Fluence Upper Limits on Different Timescales of the Four Bursts That Were Simultaneous with NICER Observations

	5 ms	10 ms	100 ms	1 s	100 s
Counts (N)	11	20	29	65	700
Count rate (counts s^{-1})	2200	2000	290	65	7
Flux (erg cm^{-2} s^{-1})	4×10^{-9}	3.5×10^{-9}	4.9×10^{-10}	1.1×10^{-10}	1.2×10^{-11}
Fluence upper limit (erg cm^{-2})	2×10^{-11}	3.5×10^{-11}	4.9×10^{-11}	1.1×10^{-10}	1.2×10^{-09}

Note. [a]For each case (5, 10, 100, 1000 ms and 100 s) we carried out multiple simulations stepwise. Each simulation run had 10,000 simulations assuming a Poisson distribution of counts in each time bin. The input value of the simulation was the total number of counts (N), which we gradually increased in steps (for each simulation run) in order to achieve a detection probability of a possible burst at 99.99% confidence for a background count rate of 0.8 counts s^{-1}. The quoted values of counts are those needed in that time interval in order for us to detect a burst at that confidence.

beyond the scope of the current paper and will be published in another work.

The mean and peak flux density of our observation to FRB 180301 range from 16–47 mJy and 28–105 mJy. The pulse width runs from 1.7–12 ms. Both of the values appear quite normal for FRB 180301. All five pulses are well above the 7σ detection threshold. The minimal S/N of 11 indicates that the chance for any burst being spurious is less than 10^{-6} given the total observation of 13 ks even if 10% of correlated noise is included.

3.2. NICER Persistent Emission Flux Upper Limits

We do not detect any excess counts in the spectra above the NICER modeled background, which implies that the spectra is entirely dominated by background. Given this fact, we used the following steps to estimate the upper limit on the persistent flux for the source, for the given duration of the observations: understanding that the observed spectra (for both the observations) are background dominated, we used the following procedure to obtain the 5σ flux upper limit on a possible source detection. We note that the average NICER background count rate in the energy range 0.2–10 keV, around the time of the bursts 4 and 5 is 0.8 counts s^{-1}, which implies a background flux of 2.2×10^{-12} erg cm^{-2} s^{-1}, using webpimms, with a power-law slope of $\Gamma = 2$, Galactic absorption column density of $N_{\rm H} = 2.83 \times 10^{21}$ cm^{-2} (HEASARC; Kalberla et al. 2005), and intrinsic absorption column of $N_{\rm H} = 10^{21}$ cm^{-2} at $z = 0.334$. A simple power-law ($\Gamma = 2$ frozen) fit to the observed time integrated spectrum of the source for observation 2 gives a 1σ error-on-background flux $= 1 \times 10^{-12}$ erg cm^{-2} s^{-1}. Hence, the net 5σ upper limit on the background, over which any signal registered can be confidently identified as a detection, can be estimated by upper limit = background flux + 5 × error-on-background flux + 20% of the background flux. Note that we assumed 20% of the background flux as systematic error, which is a conservative upper limit. Adopting the above prescription, the corresponding persistent flux upper limit is $< 7.64 \times 10^{-12}$ erg cm^{-2} s^{-1} over observations 2 and 3. The corresponding upper limit on the intrinsic persistent luminosity of the source turns out to be $L_{0.3-12\ \rm keV} < 2.50 \times 10^{45}$ erg s^{-1} for a luminosity distance of 1.7 Gpc. Note that we did not consider higher column density absorption, apart from the ones mentioned above, while estimating the X-ray flux. First, because it would be highly speculative to assume an arbitrary intrinsic absorption ($N_{\rm H}$), as we have no measurements of the quantity. Second, if we include such an ad hoc absorption column, it will only increase the estimates of the X-ray flux, pushing the value of the $\eta_{R/X}$ to lower values, making the quantity more unconstraining.

3.3. NICER Prompt Emission Flux Upper Limits

We searched carefully for any detectable X-ray counts around the radio burst arrival times, for the four strictly simultaneous bursts. NICER is the only telescope with high effective area and with high temporal resolution in X-rays capable of capturing photon events even at sub-millisecond timescales. We binned the light curve to 1 ms (typical FRB width) and searched for any photon counts in excess of 99.99% confidence for any given bin, around the burst, for time intervals of 5, 10, 100 ms, 1 and 100 s. We did not find any excess counts above the background, at $>$ 99.99% confidence. In the next step we carried out a more rigorous and realistic simulation to estimate the 99.99% confidence level of the upper limit on detection at these five different time intervals around the burst times.

We estimated the upper limit on the X-ray fluence of the four radio bursts coincident with NICER observations using simulations that take into consideration the Poisson statistics and the average background count rate (that we have measured in each instance of the FRB). We note that the NICER background count rate of 0.8 counts s^{-1} were similar for bursts 4 and 5 and this was the time range which were not affected by the SAA flaring wings, as in the cases of bursts 1 and 3. Hence, we assumed the same X-ray background count rate for bursts 1 and 3, which are contaminated by SAA entry-exit flaring wings. Therefore, we obtained only one set of upper limits for all four bursts (albeit for different time resolutions). See Table 3. Below we illustrate the steps.

Assuming a Poisson probability distribution, we estimated the total number of source counts required in order to *detect* a burst with >99.99% confidence, given a background, following the methods enumerated in Gavriil et al. (2004) and Younes et al. (2020). Since we are probing the five different timescales, we assumed the corresponding ΔT values of the bursts (i.e., T_{90}): 5, 10, 100 ms, 1 and 100 s, and with a time resolution of investigation of $\sim 1/10$ of that of the ΔT, in all the cases. This is to ensure that we are time sampling the data adequately and do not wash out the few counts in smaller time bins. We estimate the probability $_{Pi}$ of the total counts in each time bin, n_i, to be a random fluctuation around the average value (λ), which is the ratio of the total counts within ΔT over ΔT, as $P_i = (\lambda^{n_i} \exp(-\lambda))/n_i!$. The time bins satisfying the criterion $_{Pi} < 0.01/N$ are identified as a burst. The procedure is repeated until no more bins are identified in ΔT. From the total source count rate 99.99% upper limits obtained from the simulations,

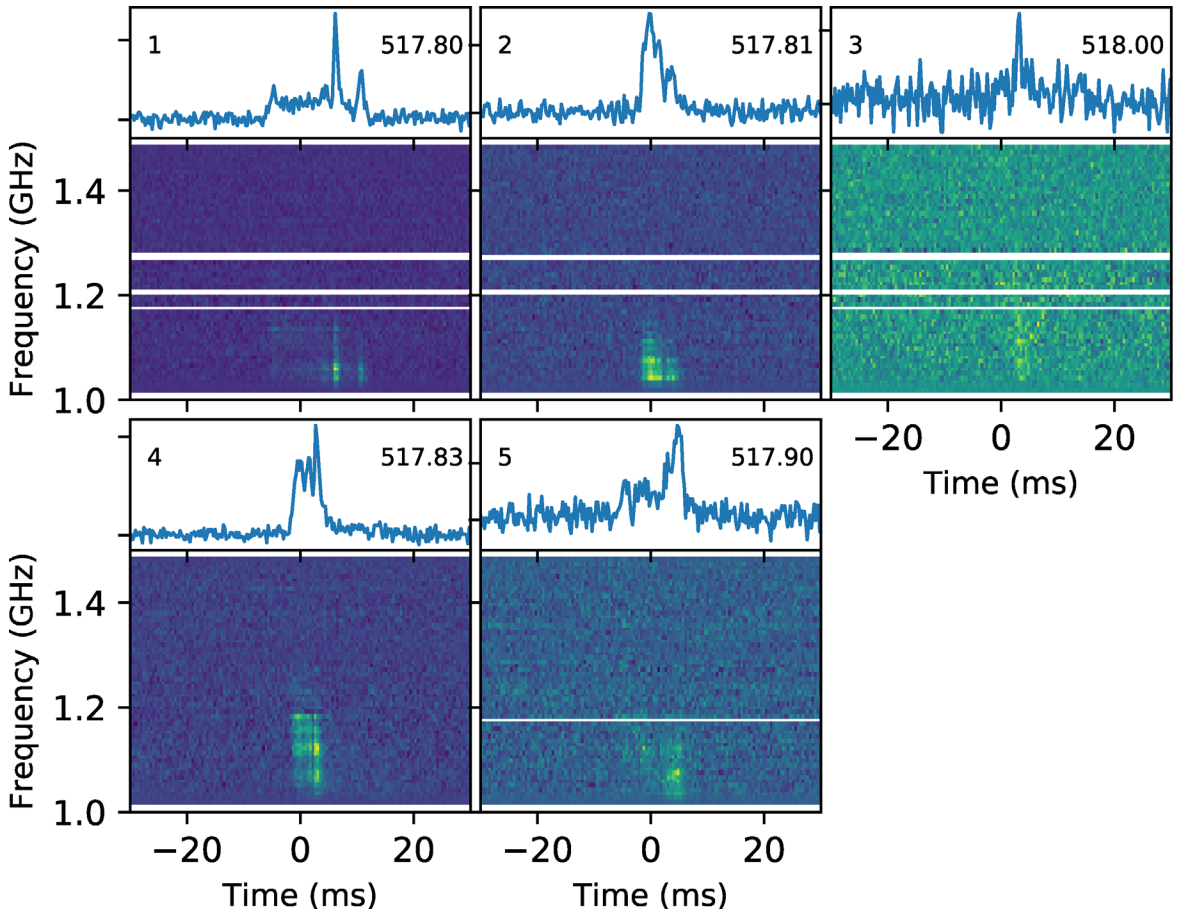

Figure 1. NICER light curve for observations 2 and 3. The *wings* in the light curve are caused by periods of enhanced particle background as NICER enters/exits the SAA, and the gaps are due to periods of Earth occultation caused by the ISS's low Earth orbit.

we converted it to flux using webpimms, assuming a spectral power-law slope of $\Gamma = 2$. The upper limits on the fluences are listed in Table 3. For the case of $\Delta T = 5$ ms we kept the time resolution = 2.5 ms. For the case of $\Delta T = 100$ s we increased the background time to 100 s, and kept the time resolution 10 s. In each case, we carried out 10,000 simulations.

3.4. Radio Efficiency η

Assuming a flat spectral index over a bandwidth of ∼200 MHz, the FRB fluences in Table 2 are $\{6, 2, 0.7, 5, 4\} \times 10^{-19}$ erg cm^{-2}. The corresponding dimensionless 10 ms transient fluence ratio lower limit is $\mathcal{F}_{\rm radio}/\mathcal{F}_{\rm X-ray} = \eta_{R/X} > \{1.7, -, 0.2, 1.4, 1.1\} \times 10^{-8}$ adopting the values in Table 3. The missing value of η corresponds to the burst FRB 2 (see Figure 2), which did not have a contemporaneous NICER observation. The 10 ms transient limit represents a case similar to SGR 1935+2154, where offsets with the radio pulses (ToAs at infinite-frequency equivalent) and features in the X-ray light curve were of order 7 ms (Mereghetti et al. 2020) and the width of the high-energy light-curve features was ∼3 ms.

On the other hand, uncertainty in the DM of order ΔDM ∼10 pc cm^{-3} may exist, which could impart temporal uncertainty of order ∼40 ms for Figure 2. However, we detect no unusual unmodeled fluctuations over background in any of the NICER snapshots consistent with activity from a cosmological source.

The radio efficiency $\eta_{R/X}$ can in principle be used to differentiate the models involving magnetospheres or relativistic shocks, with the former models predicting a higher efficiency than the latter models (Zhang 2020). The derived upper limit, generally of the order of $\eta_{R/X} > 10^{-8}$, is however too loose to place a significant constraint, so that both magnetospheric models (e..g. Wadiasingh & Timokhin 2019; Suvorov & Kokkotas 2019; Lu et al. 2020; Lyubarsky 2020; Lyutikov & Popov 2020; Wadiasingh & Chirenti 2020; Horvath et al. 2022; Yang & Zhang 2021) and synchrotron maser models involving relativistic shocks (e.g., Popov & Postnov 2010; Lyubarsky 2014; Beloborodov 2017; Metzger et al. 2019; Margalit et al. 2020 are allowed by the data.

We searched the literature extensively to find cases where (1) an X-ray instrument was observing the source when the FRB was bursting, so as to obtain an X-ray upper limit contemporaneous with a radio burst, and (2) the FRB has a distance estimate or an upper limit from the DM. Table 4 shows the list of repeating and non-repeating FRBs selected from the literature using these criteria. We also include the two soft gamma repeaters (SGRs) for comparison. One is the classic case of SGR 1935, with simultaneous radio and X-ray detection (Mereghetti et al. 2020). The other is the Galactic SGR 1806, which has shown giant flares, yet no contemporaneous

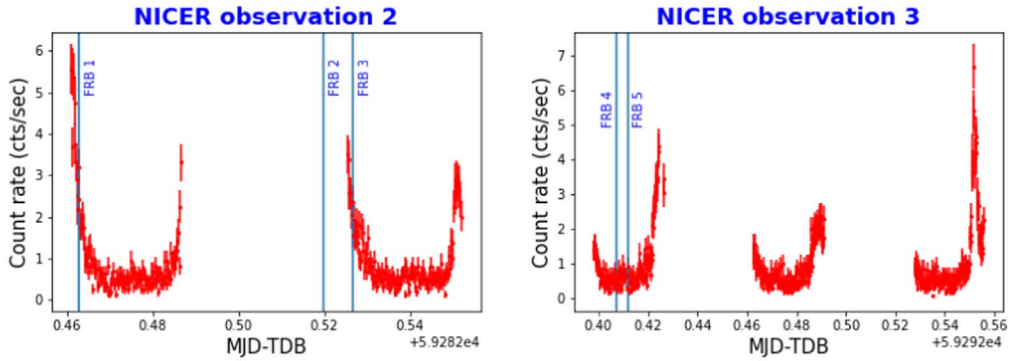

Figure 2. Pulse profile and dynamical spectra of FRB 180301 measured with FAST. The burst number (upper left panel) and DM (upper right panel) are given in each panel. White strips in the dynamical spectra indicate the RFI *zapping*.

Table 4
Detection/Upper Limits on the Fluence/Energy in Radio and X-Rays for Different FRBs

Source Type	Source[b]	Radio Fluence (erg cm^{-2}[d])	Radio Frequency	X-ray Fluence erg cm^{-2}	Distance[c] Mpc	Energy (Radio) erg	Energy (X-ray) erg
Repeating	FRB 180301[a]	6.5(−19)	1.4 GHz	<2(−11)	1700	1.68(37)	<5.20(44)
FRB	〃	0.8(−19)	1.4 GHz	<2(−11)	〃	2.12(36)	<5.20(44)
	〃	5.8(−19)	1.4 GHz	<2(−11)	〃	1.50(37)	<5.20(44)
	〃	4.3(−19)	1.4 GHz	<2(−11)	〃	1.10(37)	<5.20(44)
	FRB 121102A[1,2]	3.59(−18)	1.4 GHz	<2(−07)	949	2.92(37)	<1.62(48)
	FRB 180916[3]	8.17(−18)	⋯	<5.00(−10)	140	1.53(36)	<8.82(43)
	FRB 200120E[4]	2.28(−18)	⋯	<1.00(−08)	3	1.85(32)	<8.10(41)
Non-repeating	FRB 010724[1]	4.49(−16)	1.4 GHz	<2(−07)	<2000	<1.62(40)	<7.20(48)
FRB	FRB 110220[1]	2.4(−17)	1.4 GHz	<2(−07)	<1148	<2.84(38)	<2.37(48)
	FRB 130729[1]	1.05(−17)	1.4 GHz	<2(−08)	<2391	<5.40(38)	<1.03(48)
	FRB 010621[1]	8.7(−18)	1.4 GHz	<2(−07)	<735	<4.22(37)	<9.72(47)
	FRB 011025[1]	8.4(−18)	1.4 GHz	<2(−07)	<2029	<3.11(38)	<7.41(48)
	FRB 131104[1]	8.1(−18)	1.4 GHz	<1(−08)	<1148	<9.6(37)	<1.18(47)
	FRB 121002[1]	6.9(−18)	1.4 GHz	<1(−08)	<1558	<1.5(38)	<2.18(47)
	FRB 090625[1]	6.6(−18)	1.4 GHz	<1(−08)	<2520	<3.77(38)	<5.71(47)
	FRB 110703[1]	5.4(−18)	1.4 GHz	<1(−08)	<2980	<4.31(38)	<7.99(47)
	FRB 130626[1]	4.5(−18)	1.4 GHz	<2(−08)	<2520	<2.57(38)	<1.14(48)
	FRB 140514[1]	3.9-18)	1.4 GHz	<2(−08)	<1148	<4.62(37)	<2.37(47)
	FRB 130628[1]	3.59(−18)	1.4 GHz	<1(−08)	<1318	<5.62(37)	<1.56(47)
	FRB 110626[1]	2.1(−18)	1.4 GHz	<1(−08)	<2029	<7.78(37)	<3.70(47)
	FRB 120127[1]	1.79(−18)	1.4 GHz	<2(−08)	<1609	< 4.19(37)	<4.65(47)
	FRB 180924B[5]	4.79(−17)	⋯	<4.00(−07)	896	3.46(38)	<2.89(48)
	FRB 190714A[6]	2.4(−18)	⋯	<7.38(−08)	731	1.15(37)	<3.54(47)
	FRB 171020A[6]	1.12(−15)	⋯	<9.00(−08)	36	1.32(37)	<1.04(45)
	FRB 190523A[7]	8.39(−16)	⋯	<4.00(−07)	1298	1.27(40)	<6.06(48)
SGR	SGR 1086[1]	<3.3(−17)	1.4 GHz	1.0(00)	0.014	<5.82(27))	2.46(45)
	SGR 1935[8]	1.44(−12)	⋯	6.1(−07)	0.004	2.07(32)	8.78(37)
	〃 [9]	<3(−20)	⋯	6.8(−07)	0.004	<4.3(24)	9.00(37)

Notes.

[a] This work.

[b] References for radio and X-ray fluences. Note that we quote the upper limits of the X-ray fluence from those studies where they have been derived contemporaneously with a radio burst from the respective FRB, except for FRB 200120E from M81. [1]Tendulkar et al. (2016), [2]Bhandari et al. (2022), [3]Scholz et al. (2020), [4]Majid et al. (2021), Mereghetti et al. (2021), [5]Gourdji et al. (2020), [6]Anumarlapudi et al. (2020), [7]Prochaska et al. (2019), [8]Mereghetti et al. (2020), [9]Lin et al. (2020).

[c] References for distances: FRB 180301: Bhandari et al. (2022), FRB 121102: Tendulkar et al. (2017), FRB 20201124A: Fong et al. (2021), FRB 180916: Marcote et al. (2020). FRB 010724: Guidorzi et al. (2019), FRB 110220: Petroff et al. (2015), FRB 130729: Champion et al. (2016), FRB 010621: Keane et al. (2012), FRB 011025: Burke-Spolaor & Bannister (2014), FRB 131104: Sakamoto et al. (2021), FRB 121002: Champion et al. (2016), FRB 090625: Champion et al. (2016), FRB 110703: Thornton et al. (2013), FRB 130626: Champion et al. (2016), FRB 140514: Petroff et al. (2015), FRB 130628: Champion et al. (2016), FRB 110626: Thornton et al. (2013), FRB 120127: Thornton et al. (2013), FRBs 180924B, 190608B, 190714A, 171020A, 190523A, 18112: Bhandari et al. (2022).

[d] Conversion of jansky to millisecond fluence to erg per cubic centimeter: we know 1 Jy = 10^{-23} erg s^{-1} cm^{-2} Hz^{-1}, and we assume a bandwidth of ∼300 MHz. Hence, for example, (10^{-3} × 18 Jy) × (12 × 10^{-3} s) × (10^{-23}erg s^{-1} cm^{2} Hz^{-1} Jy^{-1}) × (3 × 10^{8} Hz) = 6.5 × 10^{-19} erg cm^{-2}. For the Parkes Telescope we used a bandwidth of 288 MHz (Tendulkar et al. 2016), and a flat spectral index, to obtain the fluence in the radio band at 1.4 GHz. For the cases where we do not know the bandwidth, we assume 300 MHz, and a flat spectral slope.

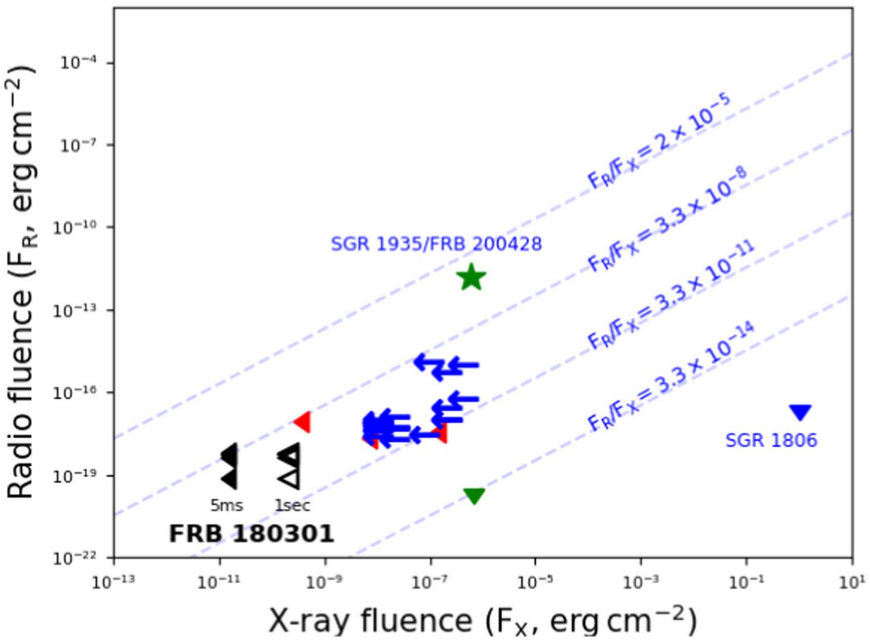

Figure 3. X-ray and radio fluence limits of the FRBs and SGRs listed in Table 4. The black solid triangles denote the X-ray upper limits of FRB 180301 from our work, using a 5 ms integration time, while the hollow triangles refer to the limits when we used a 1 s integration time. The red triangles denote the X-ray upper limits for the three other repeating FRBs listed in Table 4. The blue arrows denote the X-ray fluence upper limits of the non-repeating FRBs listed in Table 4. The green star is the contemporaneous detection in both X-rays and radio of SGR 1935/FRB 200428, while the green upper limit correspond to the radio fluence upper limits by FAST contemporaneous to 29 soft gamma bursts from SRG 1935 (Lin et al. 2020). The blue triangle in the bottom right corner of the figure denotes the radio upper limit of SGR 1806 during one of its bursting phases. References to all the studies are reported in the caption of Table 4.

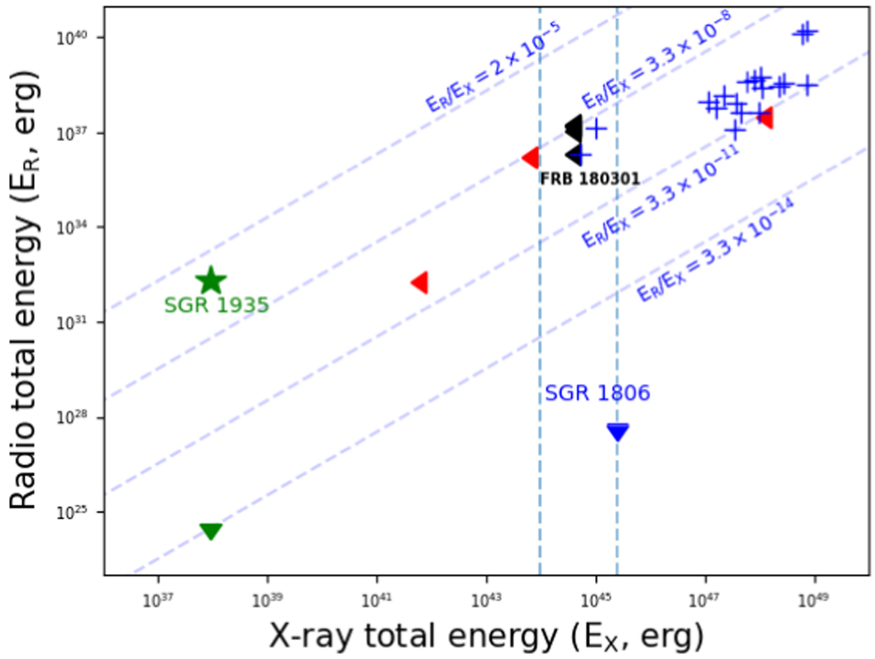

Figure 4. X-ray and radio energy limits measured for different FRBs and SGR as reported in Table 4. The black triangles denote the X-ray upper limits of FRB 180301 from our work. The red triangles denote the X-ray upper limits for the repeating FRBs listed in Table 4. The green star denotes the contemporaneous detection in either band for SGR 1935, while the green upper limit corresponds to the radio fluence upper limits by FAST contemporaneous to 29 soft gamma bursts from SRG 1935 (Lin et al. 2020). The blue triangle in the bottom right of the figure denotes the radio energy upper limit of SGR 1806. Note that for all the repeating FRBs we have proper distance estimates. We only have upper limits on distance for the non-repeating FRBs, and hence we have plotted the corresponding values as a "+" sign, which denotes the upper limit of the energy in both the X (X-rays) and Y (radio) axes. The left dashed vertical line corresponds to a total energy of 10^{44} erg, and the right dashed vertical line refers to an energy of 2.45×10^{45} erg corresponding to the SGR 1806 giant flare and other similar local giant flares (Burns et al. 2021). The references for the distances for all the sources are listed in the caption of Table 4.

signatures of FRB (Tendulkar et al. 2016), hence putting a strong upper limit on the radio fluence and energy. In Figures 3 and 4, we present the detections and upper limits of the various FRBs and SGR bursts with or without X-ray detections. In Figure 3, the black triangles (filled and hollow) are the X-ray upper limits on the four radio bursts from FRB 180301

obtained in this work. The filled triangles are upper limits corresponding to 5 ms integration time while the hollow triangles correspond to 1 s integration time (also see Table 3). This is to have a fair comparison between the different X-ray instruments used to obtain the upper limits, which have different integration times. For example, Scholz et al. 2020 obtained a 5σ prompt upper limit of $\sim 5\times10^{-10}$ erg cm^{-2} for FRB 180916, using Chandra, which has an integration time of 3 s (marked as a red triangle in Figure 3). For most of the other cases in the literature, the integration time is of the order of a few milliseconds. We plot two vertical lines in Figure 4, which correspond to the giant X-ray burst energy of the magnetars SGR 1806 ($\sim 2.5 \times 10^{45}$ erg) and SGR 1900+14 ($\sim 10^{44}$ erg), to offer a perspective of the energy involved. We find that the energy upper limits obtained from our work (black solid triangles) can rule out giant magnetar flares of the type detected in SGR 1806. However, for the non-repeating FRBs in the Figure 4 plotted as "+" (denoting upper limits in both X-rays and radio), the limits are not very constraining.

In Figure 3, the constant $\eta_{R/X}$ lines are also marked, and we can see that so far FRB 200428 from SGR 1935+2154 has the highest $\eta_{R/X}$, a value that could be interpreted within both the magnetospheric (Wang et al. 2019; Lu et al. 2020; Yang & Zhang 2021) and the external shock (Margalit et al. 2020) models. In order to make further progress to break the degeneracy between the models, simultaneous radio and X-ray observations of intrinsically bright FRBs at very small distances (in the Milky Way or very nearby galaxies) are needed.

4. Summary and Discussion

In this work, we have reported the detection of five bursts from FRB 180301 with FAST in the L band, four of which were contemporaneous with NICER monitoring of the source. The five bursts all exhibit no circular polarization, albeit with lower linear polarization than the previously reported epoch in 2019. No unusual X-ray emission over background is discernible for the four bursts, which were strictly simultaneous (after accounting for DM) with NICER observations. Nor is any emission over background detected for possible delays associated with DM uncertainty or intrinsic temporal offsets, within the duration commensurate the NICER snapshots ($\sim$1000 s). The corresponding radio-to-X-ray 5 ms fluence ratio is $\gtrsim 10^{-8}$ for the four strictly simultaneous radio bursts. An absorbed 5σ 0.3–12 keV persistent X-ray flux limit of $L_{0.3-12\ \mathrm{keV}} < 6.0 \times 10^{45}$ erg s^{-1} is also found.

A fluence of few $\times\ 10^{-19}$ erg cm^{-2} yields a characteristic isotropic-equivalent radio energy of 10^{37}–10^{38} erg, an energy scale that is typical for FRBs (repeaters and apparent non-repeaters) with accurate localizations such as FRB 121102, FRB 180924, FRB 181112, and FRB 20201124A (Tendulkar et al. 2017; Bannister et al. 2019; Prochaska et al. 2019; Kilpatrick et al. 2021; Lanman et al. 2022; Piro et al. 2021). This is consistent with models that predict a narrow universal luminosity function (e.g., Wadiasingh et al. 2020; Beniamini et al. 2020) for FRBs.

Our persistent and transient X-ray upper limits constrain any FRB progenitor to prompt radio efficiency $\eta_{R/X} \gtrsim 10^{-8}$. This is generally unconstraining for a large class of models involving stellar-mass compact objects and repetition. Ideally one would be able to distinguish between the magnetar and outflow models if an $\eta_{R/X} \geqslant 10^{-5}$ (Zhang 2020). From Figure 3 we can see that if NICER simultaneously monitors an FRB of a fluence of $\geqslant 10^{-16}$ erg cm^{-2}, then the corresponding $\eta_{R/X}$ (even for a non-detection in X-rays) can be very constraining ($\eta_{R/X} > 10^{-5}$), as has been observed in SGR 1935/FRB 200428. However, such bright FRBs are rare, and the ones that are bright enough are mostly non-repeaters (see Figure 3 left, arrows) making the task all the more difficult. Most repeating FRBs are not bright enough to pass the threshold. Hence, continuous monitoring and serendipitous discoveries are the only way that we can make progress on this subject. In the context of magnetar models, the persistent luminosity limit of $L_{2-10\ \mathrm{keV}} < 8 \times 10^{44}$ erg cm^{-1} disfavors a scenario where separate magnetar giant flares are associated with each radio burst, if they produce bright quasi-thermal pulsations as known to follow the hard spike of giant flares in nearby magnetars (Mazets et al. 1979; Cline et al. 1980; Hurley et al. 1999, 2005; Palmer et al. 2005; Burns et al. 2021). The derived upper limit on $\eta_{R/X}$ is consistent with both magnetospheric models and synchrotron maser models involving relativistic shocks. Future multiwavelength monitoring of FRB 180301 may reveal brighter bursts from this source (fluence $\geqslant 10^{-16}$ erg cm^{-2}), in which case we may be able to place stronger constraints on theoretical models.

The material is based upon work supported by NASA under award No. 80GSFC21M0002. M.N. is supported by the European Research Council (ERC) under the European Unions Horizon 2020 research and innovation program (grant agreement No. 948381) and by a Fellowship from the Alan Turing Institute.

ORCID iDs

Sibasish Laha https://orcid.org/0000-0003-2714-0487
George Younes https://orcid.org/0000-0002-7991-028X
Zorawar Wadiasingh https://orcid.org/0000-0002-9249-0515
Noel Klingler https://orcid.org/0000-0002-7465-0941
Bing Zhang https://orcid.org/0000-0002-9725-2524
Wei-Wei Zhu https://orcid.org/0000-0001-5105-4058
Ritesh Ghosh https://orcid.org/0000-0003-4790-2653
Eleonora Troja https://orcid.org/0000-0002-1869-7817
S. Bradley Cenko https://orcid.org/0000-0003-1673-970X
Samantha Oates https://orcid.org/0000-0001-9309-7873
Matt Nicholl https://orcid.org/0000-0002-2555-3192
Josefa Becerra González https://orcid.org/0000-0002-6729-9022
Eileen Meyer https://orcid.org/0000-0002-7676-9962
Tyler Parsotan https://orcid.org/0000-0002-4299-2517

References

Anumarlapudi, A., Bhalerao, V., Tendulkar, S. P., & Balasubramanian, A. 2020, ApJ, 888, 40
Bannister, K. W., Deller, A. T., Phillips, C., et al. 2019, Sci, 365, 565
Beloborodov, A. M. 2017, ApJ, 843, L26
Beniamini, P., Wadiasingh, Z., & Metzger, B. D. 2020, MNRAS, 496, 3390
Bhandari, S., Heintz, K. E., Aggarwal, K., et al. 2022, AJ, 163, 69
Bochenek, C. D., Ravi, V., Belov, K. V., et al. 2020, Nat, 587, 59
Burke-Spolaor, S., & Bannister, K. W. 2014, ApJ, 792, 19
Burns, E., Svinkin, D., Hurley, K., et al. 2021, ApJ, 907, L28
Caleb, M., & Keane, E. 2021, Univ, 7, 453
Champion, D. J., Petroff, E., Kramer, M., et al. 2016, MNRAS, 460, L30
CHIME/FRB Collaboration, Andersen, B. C., Bandura, K., et al. 2019a, ApJL, 885, L24
CHIME/FRB Collaboration, Andersen, B. C., Bandura, K., et al. 2019b, ApJ, 885, L24
CHIME/FRB Collaboration, Andersen, B. C., Bandura, K., et al. 2020, Nat, 587, 54
Cline, T. L., Desai, U. D., Pizzichini, G., et al. 1980, ApJ, 237, L1
Feng, Y., Li, D., Yang, Y.-P., et al. 2022, Sci, 375, 1266
Fong, W.-f., Dong, Y., Leja, J., et al. 2021, ApJ, 919, L23
Gavriil, F. P., Kaspi, V. M., & Woods, P. M. 2004, ApJ, 607, 959

Gendreau, K. C., Arzoumanian, Z., Adkins, P. W., et al. 2016, Proc. SPIE, 9905, 99051H
Gourdji, K., Rowlinson, A., Wijers, R. A. M. J., & Goldstein, A. 2020, MNRAS, 497, 3131
Guidorzi, C., Marongiu, M., Martone, R., et al. 2019, ApJ, 882, 100
Hickish, J., Abdurashidova, Z., Ali, Z., et al. 2016, JAI, 05, 1641001
Hobbs, G. B., Edwards, R. T., & Manchester, R. N. 2006, MNRAS, 369, 655
Horvath, J. E., Moraes, P. H. R. S., de Avellar, M. G. B., & Rocha, L. S. 2022, RAA, 22, 035004
Hotan, A. W., van Straten, W., & Manchester, R. N. 2004, PASA, 21, 302
Hurley, K., Boggs, S. E., Smith, D. M., et al. 2005, Nat, 434, 1098
Hurley, K., Cline, T., Mazets, E., et al. 1999, Nat, 397, 41
Jiang, P., Tang, N.-Y., Hou, L.-G., et al. 2020, RAA, 20, 064
Kalberla, P. M. W., Burton, W. B., Hartmann, D., et al. 2005, A&A, 440, 775
Katz, J. I. 2016, ApJ, 826, 226
Keane, E. F., Stappers, B. W., Kramer, M., & Lyne, A. G. 2012, MNRAS, 425, L71
Kilpatrick, C. D., Fong, W., Prochaska, J. X., et al. 2021, ATel, 14516, 1
Kulkarni, S. R., Ofek, E. O., Neill, J. D., Zheng, Z., & Juric, M. 2014, ApJ, 797, 70
Kumar, P., Lu, W., & Bhattacharya, M. 2017, MNRAS, 468, 2726
Lanman, A. E., Andersen, B. C., Chawla, P., et al. 2022, ApJ, 927, 59
Li, C. K., Lin, L., Xiong, S. L., et al. 2021, NatAs, 5, 378
Lin, L., Zhang, C. F., Wang, P., et al. 2020, Nat, 587, 63
Lorimer, D. R., Bailes, M., McLaughlin, M. A., Narkevic, D. J., & Crawford, F. 2007, Sci, 318, 777
Lu, W., Kumar, P., & Zhang, B. 2020, MNRAS, 498, 1397
Luo, R., Wang, B. J., Men, Y. P., et al. 2020, Nat, 586, 693
Lyubarsky, Y. 2014, MNRAS, 442, L9
Lyubarsky, Y. 2020, ApJ, 897, 1
Lyutikov, M., & Popov, S. 2020, arXiv:2005.05093
Majid, W. A., Pearlman, A. B., Prince, T. A., et al. 2021, ApJ, 919, L6
Marcote, B., Nimmo, K., Hessels, J. W. T., et al. 2020, Natur, 577, 190
Margalit, B., Beniamini, P., Sridhar, N., & Metzger, B. D. 2020, ApJ, 899, L27
Mazets, E. P., Golentskii, S. V., Ilinskii, V. N., Aptekar, R. L., & Guryan, I. A. 1979, Nat, 282, 587
Men, Y. P., Luo, R., Chen, M. Z., et al. 2019, MNRAS, 488, 3957
Mereghetti, S., Savchenko, V., Ferrigno, C., et al. 2020, ApJ, 898, L29
Mereghetti, S., Topinka, M., Rigoselli, M., & Götz, D. 2021, ApJ, 921, L3
Metzger, B. D., Margalit, B., & Sironi, L. 2019, MNRAS, 485, 4091
Michilli, D., Seymour, A., Hessels, J. W. T., et al. 2018, AAS Meeting, 231 243.18
Nan, R., Li, D., Jin, C., et al. 2011, IJMPD, 20, 989
Palmer, D. M., Barthelmy, S., Gehrels, N., et al. 2005, Nat, 434, 1107
Petroff, E., Bailes, M., Barr, E. D., et al. 2015, MNRAS, 447, 246
Petroff, E., Oostrum, L. C., Stappers, B. W., et al. 2019, MNRAS, 482, 3109
Piro, L., Bruni, G., Troja, E., et al. 2021, A&A, 656, L15
Popov, S. B., & Postnov, K. A. 2010, in Evolution of Cosmic Objects through their Physical Activity, ed. H. A. Harutyunian, A. M. Mickaelian, & Y. Terzian (Yerevan: "Gitutyun" Publishing House of NAS RA), 129
Popov, S. B., & Postnov, K. A. 2013, arXiv:1307.4924
Prochaska, J. X., Macquart, J.-P., McQuinn, M., et al. 2019, Sci, 366, 231
Sakamoto, T., Troja, E., Lien, A., et al. 2021, ApJ, 908, 137
Scholz, P., Cook, A., Cruces, M., et al. 2020, ApJ, 901, 165
Sridhar, N., Metzger, B. D., Beniamini, P., et al. 2021, ApJ, 917, 13
Suvorov, A. G., & Kokkotas, K. D. 2019, MNRAS, 488, 5887
Tendulkar, S. P., Bassa, C. G., Cordes, J. M., et al. 2017, ApJ, 834, L7
Tendulkar, S. P., Kaspi, V. M., & Patel, C. 2016, ApJ, 827, 59
Thornton, D., et al. 2013, Sci, 341, 53
Wadiasingh, Z., Beniamini, P., Timokhin, A., et al. 2020, ApJ, 891, 82
Wadiasingh, Z., & Chirenti, C. 2020, ApJ, 903, L38
Wadiasingh, Z., & Timokhin, A. 2019, ApJ, 879, 4
Wang, J. B., Coles, W. A., Hobbs, G., et al. 2017, MNRAS, 469, 425
Wang, W., Zhang, B., Chen, X., & Xu, R. 2019, ApJ, 876, L15
Xu, H., Niu, J. R., Chen, P., et al. 2021, arXiv:2111.11764
Yang, Y.-P., & Zhang, B. 2018, ApJ, 868, 31
Yang, Y.-P., & Zhang, B. 2021, ApJ, 919, 89
Younes, G., Güver, T., Kouveliotou, C., et al. 2020, ApJ, 904, L21
Zhang, B. 2020, Nat, 587, 45
Zhang, B. 2022, ApJ, 925, 53
Zhang, C. F., Xu, J. W., Men, Y. P., et al. 2021, MNRAS, 503, 5223